



Eikonal simulations for the formation and the maintenance of atmospheric gravity wave spectra

Albert Hertzog, Claude Souprayen, Alain Hauchecorne

► To cite this version:

Albert Hertzog, Claude Souprayen, Alain Hauchecorne. Eikonal simulations for the formation and the maintenance of atmospheric gravity wave spectra. *Journal of Geophysical Research: Atmospheres*, 2002, 107 (D12), pp.ACL 4-1-ACL 4-14. 10.1029/2001JD000815 . hal-01633268

HAL Id: hal-01633268

<https://hal.science/hal-01633268>

Submitted on 12 Nov 2017

HAL is a multi-disciplinary open access archive for the deposit and dissemination of scientific research documents, whether they are published or not. The documents may come from teaching and research institutions in France or abroad, or from public or private research centers.

L'archive ouverte pluridisciplinaire **HAL**, est destinée au dépôt et à la diffusion de documents scientifiques de niveau recherche, publiés ou non, émanant des établissements d'enseignement et de recherche français ou étrangers, des laboratoires publics ou privés.

Eikonal simulations for the formation and the maintenance of atmospheric gravity wave spectra

Albert Hertzog¹

Service d'Aéronomie, Verrières-Le-Buisson, France

Claude Souprayen

Centre for Atmospheric Science, Cambridge, UK

Alain Hauchecorne

Service d'Aéronomie, Verrières-Le-Buisson, France

Received 7 May 2001; revised 3 October 2001; accepted 5 November 2001; published 22 June 2002.

[1] The atmospheric gravity wave energy spectra often show power law dependencies with wavenumbers and frequencies. A simple mechanism involving off-resonant scale-separated interactions is proposed for their formation, namely the refraction of the wave packets in pseudorandom shears encountered during their vertical propagation. In the Boussinesq and rotating frame approximation the evolution of the spectral distribution of wave action is calculated within the eikonal formalism, i.e., via the simulation of the ray paths for an ensemble of elementary wave packets. The energy spectra are then easily built from the wave action spectra. Experiments are conducted where wave packets propagate away from Dirac delta function, or spectrally uniform sources at low altitudes, in realistic atmospheric background flows. The energy spectra show dependencies with the vertical wavenumber m and horizontal wavenumber k that are consistent with the most widely recognized empirical spectral models. A specific focus is given on the vertical evolution of the vertical wavenumber spectrum. The spectrum shows an invariant scaling as N^2/m^3 at large wavenumbers. It possesses a central wavenumber whose value depends on the total wave energy and is controlled by the statistics of the background mean flow. Similarly, the wave packet azimuths show an increasingly strong anisotropy resulting from the wave mean flow interaction at critical levels.

INDEX TERMS: 3384 Meteorology and Atmospheric Dynamics: Waves and tides; 3367 Meteorology and Atmospheric Dynamics: Theoretical modeling; 3334 Meteorology and Atmospheric Dynamics: Middle atmosphere dynamics (0341, 0342); 0342 Atmospheric Composition and Structure: Middle atmosphere—energy deposition; **KEYWORDS:** gravity wave, quasi-universal spectra, ray tracing, wave refraction

1. Introduction

[2] The interpretation of the quasi-universal distribution of energy in the atmospheric gravity wave spectra and the real fluid-dynamical process or processes leading to what has been termed “wave saturation” are still questions that are open to debate. In practice, “saturation” means the occurrence of a m^{-3} asymptotic law (tail) in the vertical wavenumber energy spectrum. Many observations with balloons and radar/lidar systems show spectra with quasi-universal shapes and intensities regardless of the geographical location and time [Allen and Vincent, 1995; Smith *et al.*, 1987; Fritts *et al.*, 1988; Sidi *et al.*, 1988; Tsuda *et al.*, 1989]. Therefore several empirical models have been built in order to synthesize such observations [Smith *et al.*, 1987; Sidi *et al.*, 1988; Fritts and VanZandt, 1993]. They all

depend on a small set of parameters, each weakly varying with the altitude and the location, such as a wavenumber cutoff, the total energy, and the slopes of the asymptotic power laws. On one hand, such models are particularly useful when trying to parameterize the net long-term effect of the wave mean flow interaction, as far as energy and momentum flux deposition can be calculated. On the other hand, these statistical descriptions do not provide enough information on the mechanisms involved in the energy transfer. Several internal processes (among them, wave breaking, resonant triad interaction, radiative damping, and turbulent and eddy diffusion) have been proposed to explain the equilibrium in a wave field subject to forcing (at sources level) and sinks (presumably at small scales). All of these processes have been studied separately and in detail and are likely to be important, although each in different spectral and altitude ranges. However, up to now none of those have provided a convincing theoretical basis for the formation and the maintenance of the energy spectra.

[3] In this paper, we limit our study to a single process, the off-resonant nonlinear interaction between the waves

¹Now at Laboratoire de Meteorologie Dynamique, Palaiseau, France.

and a scale-separated background flow. For a background flow produced by both long waves and balanced motion (baroclinic eddies), the interaction can be studied within the WKB approximation with the eikonal theory [Henyey and Pomphrey, 1983]. More specifically, we use ray techniques to calculate the spatial and spectral evolution of distributions of wave action and wave energy. Such techniques have been already developed in the atmospheric context, e.g., for the analysis of the geographical gravity wave patterns produced by planetary-scale winds [Dunkerton, 1984; Dunkerton and Butchart, 1984] and for the study of the eikonal approximation (scale separation, stationarity, etc.) [Eckermann, 1997; Walterscheid, 2000]. In the oceanic context, Broutman [1986] and Broutman *et al.* [1997] gave accounts of the refraction of short-scale wave packets by inertial waves including the occurrence of caustics. In this our main purpose is to show that the interaction captured by the ray techniques produces an efficient net spectral transfer of wave energy and is almost entirely responsible for the formation of the observed spectra. Our results rely on the numerical implementation of the ray equations in a box model in which the background flow is provided by the analyses of the European Center for Medium-Range Weather Forecasting (ECMWF) model. Those equations enable the following of the evolution of the wave packets in the physical space (i.e., trajectories) and in the spectral domain (i.e., refraction).

[4] The paper is organized as follows. We devote section 2 to a short review of the most popular descriptions for the wave field. This will serve to refer the reader the various paradigms that were proposed to explain the observed shapes of gravity wave spectra in the atmosphere. The general framework for the eikonal description is provided in section 3 with a discussion on the necessary assumptions. Section 4 contains a description of the numerical details in the box model. For the different experiments that have been conducted, the initial conditions are also reported along with the method for the numerical evaluation of the spectra. General diagnostics from the numerical experiments are made in section 5 for the wave action and energy transport. In particular, we present typical ray trajectories and also discuss the marginal occurrence of reflection. Then the one-dimensional (1-D) energy spectra are constructed from the ray trajectories, and we identify the main mechanism responsible for the shaping of the spectra. In section 6 we put the emphasis on the robustness of the results for the vertical wavenumber spectrum and compare such spectrum with (1) semiempirical and observational models and (2) the theoretical analytical spectrum as described by Souprayen *et al.* [2001] with a purely stochastic approach. Section 7 is devoted to a summary of the most important results obtained with the eikonal approach.

2. Possible Mechanisms for Wave Saturation

[5] Historically, the saturation of gravity wave spectra has been attributed to the linear instability of a wave or a superposition of waves [Dewan and Good, 1986; Smith *et al.*, 1987]. The onset of convective or dynamical instability for large-amplitude fluctuations results in gravity wave breaking and acts as a limitation for further growth of the amplitude with altitude. In order to account for the m^{-3}

spectral variation of the energy density (where m is the vertical wavenumber), the saturated variance that scales as m^{-2} must be distributed on a spectral bandwidth, which is supposed to be proportional to the central wavenumber of the wave packet, $\Delta m \approx m$. The physical meaning of this statement is that any wave packet is made of a given and constant number of oscillations. The arbitrary nature of this choice is one of the several criticisms that have been made by Hines [1991a], added to the fact that $\sim 70\%$ of the saturated wave field should undergo nonlinear interactions. More recently, Dewan [1997] tried to relax the abovementioned hypothesis for the spectral bandwidth using a similitude cascade argument.

[6] Another successful explanation for the spectra has been given by Weinstock [1990]. Following a statistical description of the wave field perturbations formerly developed by Weinstock [1976], Weinstock [1990] achieved the diffusive theory that establishes an equilibrium spectra in the nonlinear regime. This is one of the seldom theories that gives an explicit and quantitative explanation for the -3 slope at large wavenumbers for the energy spectra. Weinstock [1990] applies techniques employed in turbulence statistics, such as the direct interaction approximation, in order to estimate a scale-dependent diffusion closure for the wave-wave interaction. Equating the energy flux and the diffusion term in the equilibrium state leads to the power law variation for the energy spectra.

[7] It is noteworthy that while the wave-wave interaction is accounted for by oceanographers mostly through resonant triad interactions, this mechanism has been invoked for atmospheric waves only recently Daubner and Zeitlin [1996]. The analysis is restricted to a 2-D wave field problem, but an extension to the 3-D problem, including the interaction with the vertical mode, is in progress (V. Zeitlin, personal communication, 2000).

[8] Finally, Hines [1991b] has developed a statistical approach for the wave-wave interaction through the Doppler shift effect. By assuming simple statistics for the wave-induced horizontal wind statistics, Hines calculates a diffusion function applied to arbitrary input spectra. However, this theory does not predict a universal shape for the vertical wavenumber spectrum as far as it is strongly dependent on the input spectrum. In the eikonal approach used in this paper the wave field evolves only via off-resonant interactions. The refraction that results from such interactions leads to an ensemble transport of wave action and energy from larger to smaller scales. The study provided in this article is based solely on the estimate of such an effect, as obtained from ray calculations.

3. Eikonal Formalism

[9] In this section we recall the assumptions needed for the eikonal formalism to be valid. Situations where the eikonal approach has to be questioned are reported at the end of this section and in Appendix C. Our objective is to derive a transport equation for the evolution of the wave field. It can be shown that in a time-varying (inhomogeneous) flow, the energy (\mathcal{E}) (pseudomomentum (\vec{P})) carried by a wave packet varies during its nondissipative propagation. In contrast, the wave action (\mathcal{A}) is conserved. Therefore we focus on the wave action transport rather than on

the energy transport. Energy and pseudomomentum spectra can be reconstructed from the action spectrum using the following relations [Whitham, 1974],

$$\begin{aligned}\varepsilon &= \omega A \\ \vec{P} &= k \vec{A},\end{aligned}\quad (1)$$

where ω and \vec{k} represent the wave packet intrinsic frequency and wave vector, respectively.

3.1. Basic Assumptions

[10] For the eikonal theory to be valid, a separation between the background field characteristic scales and the characteristic scales of the wave packet (e.g., central wavelength) are required. The technique amounts to solving the interaction of individual wave packets with the background flow. The mean evolution of the whole wave field is obtained by ensemble averaging on all wave packets. Therefore the mechanism enters the WKB framework, and the interaction relies on the long-wave/short-wave scattering.

[11] A further assumption is that the background flow follows an independent evolution equation or, equivalently, that the nonlinear feedback of the waves is neglected. Finally, we neglect any dissipative process for the waves along the ray trajectories. At first sight this assumption might seem unrealistic. However, in our numerical implementation we stop some of the wave trajectories that have been strongly refracted by the mean flow. This procedure somewhat mimics the dissipation of waves with small vertical scales (regardless of the exact mechanism).

3.2. Transport Equations

[12] As quoted earlier, the starting point of the theory is the conservation of the wave action in time-dependent and inhomogeneous media. The related equation, which was given by Bretherton and Garrett [1968] and Whitham [1970], reads

$$\begin{aligned}\partial_t A(\vec{x}, t) + \nabla_x \left[\vec{C}_g A(\vec{x}, t) \right] &= 0 \\ \frac{d\vec{x}}{dt} &= \vec{\nabla}_k \omega_0 = \vec{C}_g \\ \frac{d\vec{k}}{dt} &= -\vec{\nabla}_x \omega_0,\end{aligned}\quad (2)$$

where A is the wave action density in the 3-D (spatial) phase space, \vec{C}_g is the group velocity (defined as $\vec{C}_g = \nabla_k [\omega_0(\vec{k}, \vec{x}, t)]$), and ω_0 is the absolute frequency. The time derivatives of \vec{x} and \vec{k} are along the ray path of the wave packet.

[13] We need to build an equivalent transport equation not only for a single wave packet but also for the whole wave field. Therefore, applying a “weak turbulence” approximation, we describe the wave field as a superposition of wave packets. It is convenient, using techniques employed in plasma physics, to lift the wave action density in an augmented 6-D phase space (\vec{x}, \vec{k}) , where \vec{k} is considered as an independent variable. This formalism has been employed recently with success in 2-D turbulence studies [Dubrulle and Nazarenko, 1997] and in works on isentropic transport of stratospheric tracers [Haynes and Anglade, 1997]. The technical details of the derivation are

provided in Appendix A. In the 6-D phase space the wave action is given by its density $\mathcal{A}(\vec{x}, \vec{k}, t)$, and its evolution equation is

$$\partial_t \mathcal{A}(\vec{x}, \vec{k}, t) + \vec{x} \cdot \vec{\nabla}_x [\mathcal{A}(\vec{x}, \vec{k}, t)] + \vec{k} \cdot \vec{\nabla}_k [\mathcal{A}(\vec{x}, \vec{k}, t)] = 0. \quad (3)$$

[14] Given an initial distribution for the wave action density at time t_0 , say $\mathcal{A}^0 = \mathcal{A}(\vec{x}, \vec{k}, t = t_0)$, one can calculate its distribution for any time by evolving \mathcal{A}^0 conservatively along ray paths, which are the characteristics of equation (3). In the following numerical simulations we apply a Monte Carlo integration method using random ray paths.

[15] Furthermore, in the context of Boussinesq approximation in a rotating frame, the gravity-wave dispersion relation is

$$\begin{aligned}\omega^2 &= \frac{N^2(k^2 + l^2) + f^2 m^2}{k^2 + l^2 + m^2} \\ \omega_0 &= \omega + \vec{k} \cdot \vec{u}.\end{aligned}\quad (4)$$

[16] The related ray equations (system 2) are detailed in Appendix B. The time and space variations of the background flow enter the equations through N , the Brunt-Väisälä frequency, and \vec{u} , the velocity field. In the latter the vertical velocity component will be neglected (hereinafter, \vec{u} will denote the horizontal wind component). The consequences of such an approximation are discussed by Eckermann [1997] and Walterscheid [2000]. Furthermore, we keep the Coriolis parameter f constant along the rays.

4. Description of the Numerical Model

[17] In the following sections we report on the numerical implementation of the ray equations. We also describe the background fields and the method for the construction of the 1-D and 2-D spectral evolution of the wave energy density. Finally, we discuss the initial conditions of the experiment that have been conducted.

4.1. Background Fields and Numerical Integration

[18] In order to study the transport and dispersion of the wave packets, we need to prescribe the background flow. In their simulation of oceanic waves, Henyey and Pomphrey [1983] have constructed such a flow from the spectral model from Garrett and Munk [1975].

[19] Here we adopt another approach by using real synoptic-scale flows provided by the ECMWF model analyses. Ideally, the background field should contain the fluctuations produced by the large-scale component of the wave field. It is only partially true for the ECMWF analyses (using the T106 resolution, the horizontal and time scales for the flow are small enough to include some inertia-gravity wave components). Actually, we suppose that the mean transport of energy, as estimated when computing the ensemble average, does not depend on the exact statistics of the background field but rather on its pseudorandom nature along the wave packet trajectories. This statement is supported by the results obtained with the purely 1-D stochastic model [Souprayen et al., 2001].

Table 1. Characteristics of the ECMWF Fields and Initial Wave Distributions

| Parameter | Value |
|------------------------------|--|
| <i>ECMWF</i> | |
| Longitude | $[-40^\circ, 30^\circ]$ |
| Latitude | $[30^\circ, 60^\circ]$ |
| Altitude, km | $[0, 30]$ |
| Time | 18–21 February 1998 |
| Horizontal resolution | 1.125° |
| Vertical resolution | 31 layers |
| Time resolution | 6 h |
| <i>Source at 2 km</i> | |
| Longitude | $[-24^\circ, 14^\circ]$ |
| Latitude | $[34^\circ, 54^\circ]$ |
| Horizontal grid | $2^\circ \times 2^\circ$ |
| Wavenumbers, cycles m^{-1} | |
| Vertical | $[5 \times 10^{-5}, 1.6 \times 10^{-3}]$ |
| Horizontal | $[1 \times 10^{-7}, 1 \times 10^{-4}]$ |
| Intrinsic angular frequency | $[f, 6f]$ |
| Azimuth distribution | isotropic |

[20] The calculations are made in a 3-D box centered on the northern midlatitudes with horizontal dimensions given in Table 1. The time and space resolution for the wind and temperature fields is also reported. In the course of the numerical integration, cubic splines are performed in order to interpolate the background fields at the wave packet position. It also provides the first- and second-order derivatives for both the wind and the Brunt-Väisälä frequency.

[21] The starting day (February 1998) corresponds to a wintertime meteorological condition with a strong synoptic-scale wave activity to ensure the randomness of the fields. The flow near the tropopause (200 hPa) is depicted

in Figure 1 and presents a strong and meandering tropospheric jet. The maximum duration for the calculation is 3 days.

[22] The rays are launched at a constant altitude above the boundary layer (to ensure a stable stratification) and on a regular $2^\circ \times 2^\circ$ horizontal grid in the center of the ECMWF domain. In doing so, we aim at simulating an arbitrary and spatially homogeneous distribution for the sources. At each location, four azimuths of propagation are used, and for each azimuth, 10 random pairs of intrinsic frequencies and vertical wavenumbers (ω, m) are selected from uniform distributions (bounds are reported in Table 1). (Note that the lower limit for vertical wavenumbers may be questionable with regard to the WKB approximation. However, it will be shown, e.g., in section 6.1, that the waves with large vertical wavelengths are not those that are important for the mechanism that we describe in this paper.) The total number of rays is 8800. Selecting opposite signs for m and ω , we prescribe only initially upward propagating wave packets. The initial horizontal wavenumber is calculated from the dispersion relation (4), and the absolute frequency is recovered from the wind velocities at the initial position.

[23] The system of equations for the rays B1 (and when applied, for the amplitude or ray tube C1) is integrated with a fourth-order Runge-Kutta scheme with an adaptive time step. During the integration the physical and spectral characteristics of each wave packet are stored at regular altitude intervals (100 m). There are two situations when the numerical integration has to be stopped, when the time step is < 1 s and when the wave packet exits the box domain. In the first case the time step has been decreased because the rate of variation of at least one of the wave characteristics is very large. This is usually due to fast variations of the

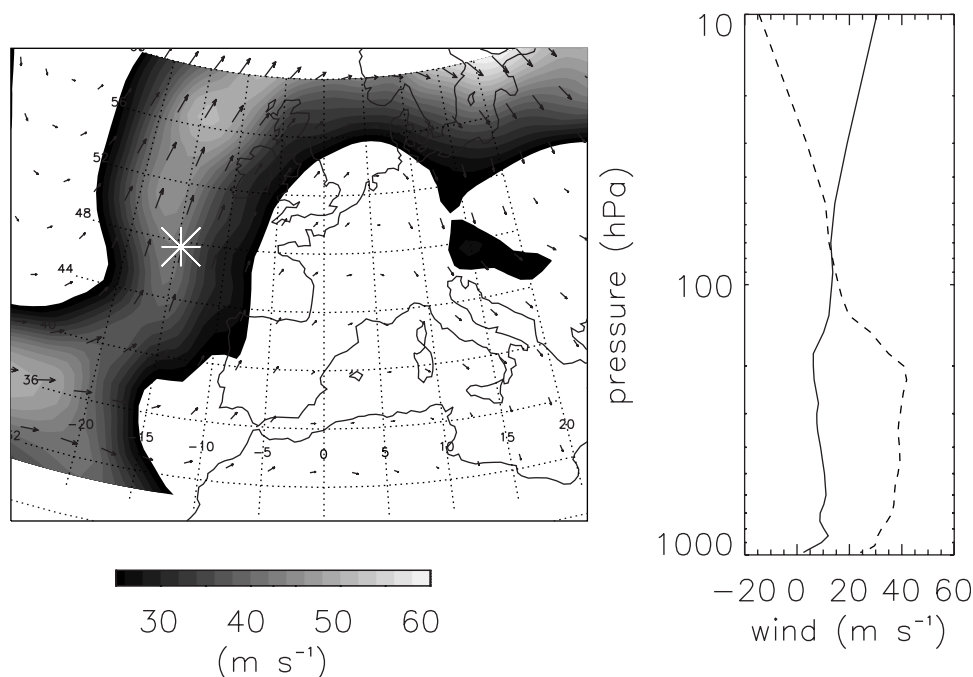


Figure 1. Flow structure in the ECMWF analyses on 20 February 1998 at 0000 UT. (left) Contours of the wind intensity at 200 hPa (velocities larger than $25 m s^{-1}$ have been shaded). (right) Vertical profile of the zonal (solid) and meridional (dashed) components at the geographical location (star).

background flow that correspond to the breakdown of the WKB approximation. Actually, a small number of such stopped rays is observed (<2%).

[24] The wave packets that exit the domain are forever discarded from the statistics that we compute. Those exit events can be split into two categories. On one hand, it can correspond to waves whose propagation is weakly disturbed. This case may occur for the waves that are launched close to box sides and exit through them or for the waves whose vertical propagation was not inhibited and exit the domain through its top boundary. On the other hand, lateral exits are often associated with the almost horizontal propagation of the large m waves. In this case, discarding those waves from our statistics may be considered as a proxy for dissipation near critical levels. This last point is discussed further in section 5.

4.2. Experiment

[25] A single experiment has been conducted. It helps gain insight into the wave field equilibrium that results from continuously emitting sources located in the lower troposphere and sinks at large wavenumbers (dissipation). To design such a simulation, however, we should have launched rays at regular time intervals and analyzed the output at later time, waiting for the equilibrium to be achieved. Rather, we used another approach by prescribing an impulsive source at $t = 0$ and by applying an ergodic assumption. In this way we can estimate the stationary spectral distributions by integrating in time the wave characteristics as observed along the trajectories. (Note that, in this context, we should not have discarded the waves that exit the domain through its sides without being refracted toward large m . We have, however, checked that similar results to those presented in the following are obtained if we only use in our statistics the waves that are launched far away from the sides; in other words, our conclusions are not determined by the fact that we are working in a box with a finite horizontal extension.) Though stationary, the spectral distributions that we obtain are not homogeneous since they exhibit strong variations with altitude. We are going to study in detail the shaping of the spectra from the arbitrary sources distributions to the observed distributions in the upper layers.

[26] As reported above, the initial vertical wavenumbers and intrinsic frequencies for the emitted wave packets are uniformly distributed in some bounded intervals. Therefore the value of the individual wave action A_i^0 at the source level can be freely chosen and determines the shape of the source spectra. In sections 5 and 6 we discuss basically two types of source spectra, large-band spectra (with various spectral slopes) and Dirac-like distributions where A_i^0 is nonzero only for a small region of m about m_0 , the central wavenumber of source.

4.3. Derivation of the 1-D Spectra

[27] We use the Lagrangian conservation of the wave action along the ray in the 6-D phase space to calculate the evolution of the action density distribution $\mathcal{A} = (\vec{x}, \vec{k}, t)$. Thus, at any time, this distribution can be reconstructed from the joint probability distribution function (pdf) for the characteristics (position and wavenumbers) of the wave packets. For instance, if we consider N wave packets with initial action A_i^0 ,

$i = 1, 2, \dots, N$ and calculate their trajectories $(\vec{x}_i(t), \vec{k}_i(t))$, the action density at later time is given by

$$\mathcal{A}(\vec{x}, \vec{k}, t) \Delta \vec{x} \Delta \vec{k} = \sum_{i=1}^N A_i^0 H[\vec{x}, \vec{x}_i(t), \vec{k}, \vec{k}_i(t)], \quad (5)$$

where the characteristic function $H[\vec{x}, \vec{x}_i(t), \vec{k}, \vec{k}_i(t)]$ is equal to 1 if $[\vec{x}_i(t), \vec{k}_i(t)]$ is in the volume $\Delta \vec{x} \Delta \vec{k}$ centered on (\vec{x}, \vec{k}) and 0 otherwise. Similarly, the energy distribution is obtained by the substitution of A_i^0 by $\omega(\vec{x}_i, \vec{k}_i) A_i^0$ in the above formula. For example, to compute the vertical wavenumber energy spectra in a given altitude layer, we use the time-integrated version of equation (5),

$$E(m, z) \Delta m \Delta z = \sum_{i \in \mathcal{I}} \omega(\vec{x}_i, \vec{k}_i) A_i^0, \quad (6)$$

where the ensemble \mathcal{I} is a restriction of all the trajectory points to the subspace $[m - \Delta m/2, m + \Delta m/2] \cap [z - \Delta z/2, z + \Delta z/2]$. In section 5 we apply this technique to build the energy spectra with respect to horizontal wavenumbers $\sqrt{k^2 + l^2}$, apparent and intrinsic frequencies, and azimuths of propagation.

5. Numerical Results

[28] First, we provide a general and qualitative overview of the trajectories and their refraction in the physical space. Then we discuss the quantitative estimate of the 1-D and 2-D energy spectra and their evolution with altitude. Finally, we identify what we believe to be the essential mechanism responsible for the energy transfer between scales in the wave field and therefore the resulting spectral shapes.

5.1. General Overview

[29] The output from the model consists in complex trajectories in a high-dimensional phase space. In this section we only show and analyze the wave packet positions in the physical space (Figure 2). A small subset of the 8800 rays is plotted in this figure, and each ray is color coded according to the value of the wave intrinsic frequency.

[30] Two dominant behaviors are roughly observed, wave packets propagating freely upward through the top of the domain and wave packets strongly horizontally refracted that are exiting the domain through its lateral sides. Accordingly, the intrinsic frequencies are strongly modified toward higher values (red rays) for the faster, almost vertically propagating waves and toward smaller values for those waves for which vertical propagation is inhibited (black rays). Most of the refraction processes occur essentially in the layers close to the strong and meandering tropospheric jet. The refracted waves become quasi-inertial with a very small intrinsic group velocity; therefore, they are passively advected by the horizontal background wind. The beam of black rays in Figure 2 roughly indicates the position and direction of the jet (compared with Figure 1).

[31] We selected a small number of specific rays corresponding to wave packets that have been reflected vertically. Their trajectories in the altitude-time domain are shown in Figure 2. Those reflections occur when the refraction produces high-frequency waves ($\omega \sim N$) as seen

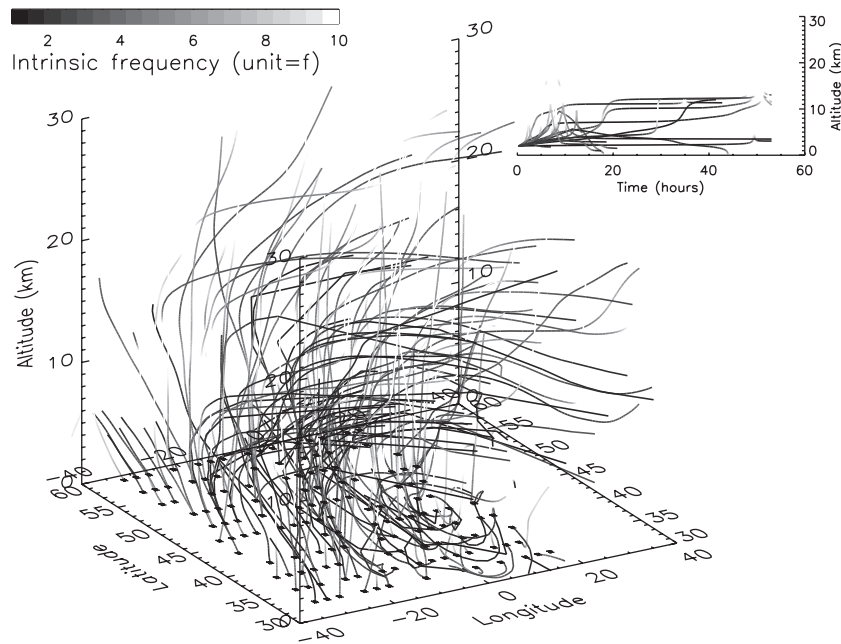


Figure 2. Arbitrary subset (2%) of wave packets trajectories. The crosses at 2 km altitude indicate the source locations, and the color index is related to the wave intrinsic frequencies. Some wave packets are refracted horizontally at the tropospheric jet level and toward low frequencies (shown in black); other waves are refracted toward high frequencies (shown in red) and are propagating freely upward. Upper right corner shows an arbitrary subset of wave packets trajectories $z = f(t)$ that shows vertical reflections. See color version of this figure at back of this issue.

on the red part of the trajectories. It happens also at the tropospheric (and stratospheric) jet level.

[32] We also want to emphasize the fact that some refracted low-frequency waves can eventually escape the jet level after a long period and propagate freely upward (see, for example, those trajectories in Figure 2 with long horizontal sections). Those escapes are made possible thanks to the nonstationarity of the background flow. For such waves the related variation from large to small vertical scales is reversible, which means that the associated energy spectral transfer is not unidirectional. However, real atmospheric waves for which the vertical propagation is inhibited for a long period are likely to be dissipated (either by radiative or turbulent processes). In that sense the removal from the statistics of wave packets that are exiting the domain through the lateral boundaries (mainly low-frequency refracted waves) somewhat mimics the real dissipative process at small scales.

5.2. Energy Spectra

[33] In this section we study the variation with altitude of the energy spectra with respect to the vertical and horizontal wavenumbers and intrinsic frequency. A unique source distribution is chosen. The initial energy joint spectrum at any geographical location is expressed as

$$E(m, \omega) = E_0 A(m) B(\omega), \quad (7)$$

with $E_0 = 1 \text{ J kg}^{-1}$. $A(m)$ and $B(\omega)$ are normalized uniform distributions (white spectra) in the spectral ranges $5 \times 10^{-5} < m \text{ (cycles m}^{-1}) < 1.6 \times 10^{-3}$ and $f < \omega < 6f$, respectively. The total altitude domain is split in adjacent layers with

increasing depth (in order to compensate for the decrease in the number of wave packets entering the statistics). The spectra are normalized accordingly. Finally, to account for the exponential decrease of the density, the individual wave packet energy per unit mass is multiplied along the trajectory by the factor $\exp(z/H)$, with $H = 7 \text{ km}$.

5.2.1. Vertical wavenumber spectrum

[34] The result for the vertical wavenumber energy spectrum is shown in Figure 3a. The striking feature is the shaping of the distribution toward the observed “universal” spectrum just above the source level.

[35] Namely, at large wavenumbers, the spectrum exhibits a m^{-3} asymptotic tail down to the largest wavenumber retained (note that this limit is unrealistically within the stratospheric turbulent range). Furthermore, the spectral magnitude at large wavenumbers varies weakly with altitude despite the increase of energy for the individual wave packets. For comparison, the $N^2/6m^3$ model of *Smith et al.* [1987] is also plotted in Figure 3. Those characteristics are classically referred to as the saturated regime for the wave field.

[36] Conversely, the spectral level at low wavenumbers is increasing with altitude, and a central wavenumber is emerging. This central wavenumber varies with altitude and is similar to m_* , which is a key parameter in most of the empirical spectral models.

[37] Finally, the total energy for each layer (provided in the plot) is increasing with altitude. Several processes can explain the small change in energy between the last two layers; it may be related either to the vertical structure of the mean flow (with alternate mean vertical shear above and below the jet) and/or to the diminution of the number of

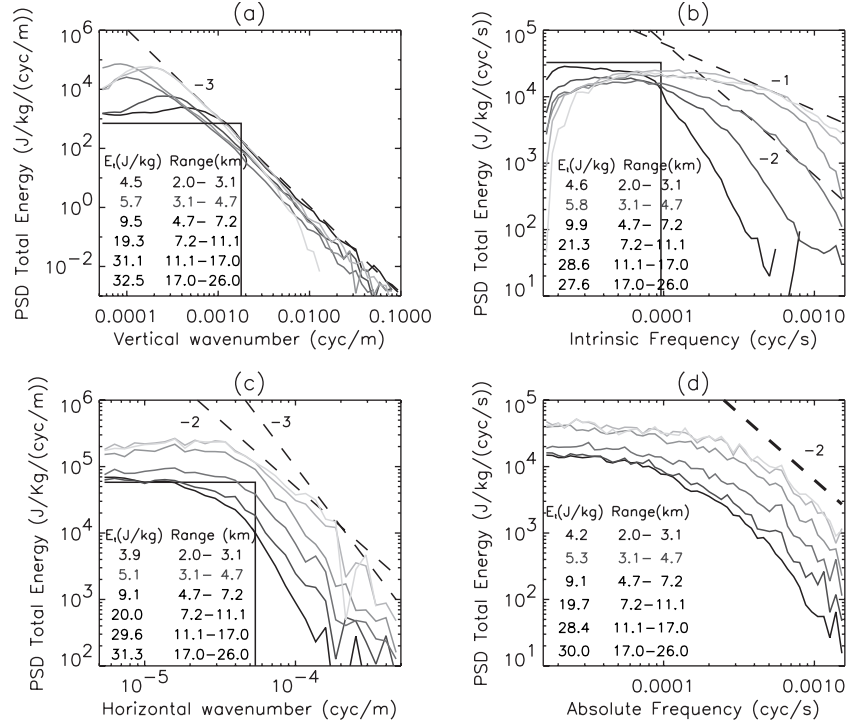


Figure 3. Altitude evolution of the 1-D energy spectra versus (a) vertical wavenumbers, (b) intrinsic frequencies, (c) horizontal wavenumbers, and (d) absolute frequencies. Launch spectra are step functions (solid black line). The colors correspond to the several adjacent vertical layers (whose thickness is increasing). The total energy per unit mass is estimated by integration of the numerical spectrum for each layer. (Note that the total energies slightly differ between each plot since the spectral ranges are not exactly overlapping.) Reference spectra are shown (dashed lines), with slopes detailed in each plot. In Figure 3a thereference spectrum corresponds to the $N^2/6m^3$ tail [Smith *et al.*, 1987]. See color version of this figure at back of this issue.

surviving wave packets above the jet. Note also that the spectral tail for the uppermost layer is departing from the expected shape, which is likely due to the limited vertical resolution of the ECMWF data in that layer.

5.2.2. Intrinsic and absolute frequency spectra

[38] In a similar way we present the variation of the intrinsic frequency energy spectrum in Figure 3b. The initial or source spectrum is quickly and strongly modified at upper levels. However, the spectra do not exhibit any clear power law. Rather, there is a general spreading of the distribution, which is reminiscent of the behavior found in the stochastic model from Souprayen *et al.* [2001]. In this 1-D model with constant horizontal wavenumber, the intrinsic frequency is proportional to the vertical wavelength and undergoes a diffusion process. Therefore the diffused spectrum strongly depends on the shape of the source spectrum at high frequencies.

[39] The decrease of the spectral levels at low frequencies ($\sim f$) can be attributed to dissipation processes near critical levels. Besides, it is important to note that, although spectral slopes as -1 , $-5/3$, and -2 are usually reported, the intrinsic frequency spectrum has never been observed in the atmosphere until recently, as far as it requires Lagrangian observations. Yet recent long-duration isopycnic balloon experiments, conducted in the equatorial lower stratosphere, seem to confirm the -2 spectral slope of the intrinsic frequency spectrum [Hertzog and Vial, 2001].

[40] The absolute (ground-based) frequency spectrum is shown in Figure 3d. Studies based on radar and lidar observations have reported spectral slopes between $-5/3$ and -2 for the absolute frequency spectrum [e.g., Gage and Nastrom, 1985; Senft *et al.*, 1993; Hertzog *et al.*, 2001]. The spectra that we obtain actually exhibit spectral slopes close to -2 in the high-frequency domain. Yet the power law behavior is not observed at periods larger than a few hours, which is at odds with observations. We shall, however, stress that the temporal resolution of the fields that we use in the simulations is relatively poor (i.e., 6 hours). Consequently, this can seriously prevent spectral transfers in the frequency domain (see equation (8)), and may explain part of the discrepancies between the observations and our results.

5.2.3. Horizontal wavenumber spectrum and anisotropy

[41] We use the total horizontal wavenumber distribution along the rays to calculate the energy spectrum as provided in Figure 3c. From the dispersion relation, and the initial source spectrum as expressed earlier in section 5.2, it can be shown that the initial k spectrum is uniform in the interval $[0, 5.10^{-5} \text{ cycles m}^{-1}]$. We show the spectra for $5.10^{-6} < k$ (cycles m^{-1}) $< 5.10^{-4}$, which covers simultaneously the source distribution and higher wavenumbers. As for the vertical wavenumber spectrum, there is a strong modification of the source spectrum. Spectral power law scalings

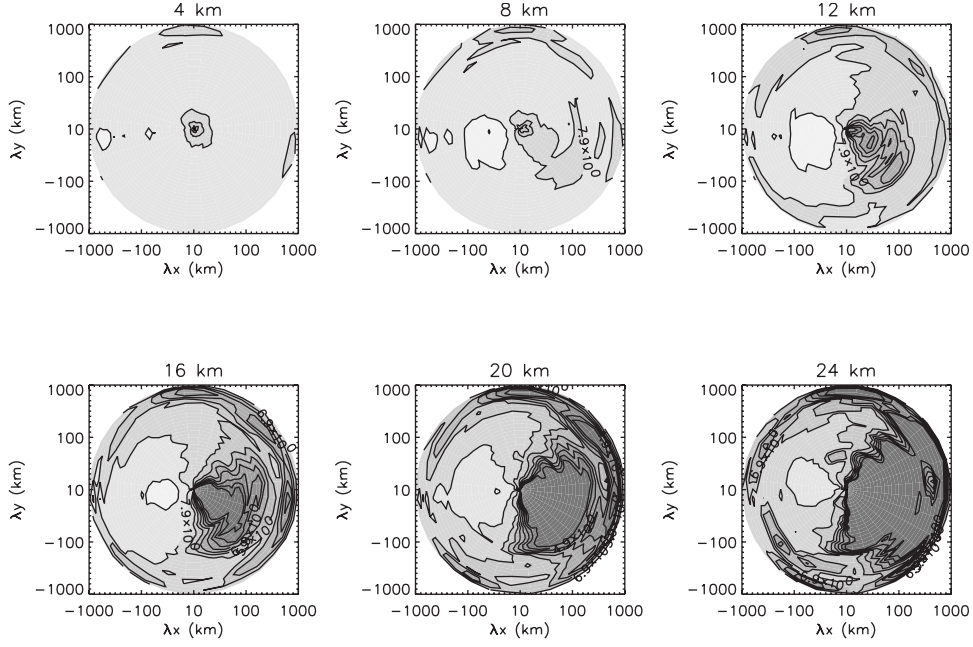


Figure 4. Two-dimensional (azimuth) energy distributions with horizontal wavelengths. The axis and the color index are in log scale, and each map corresponds to a 4 km depth layer centered at the indicated altitude. Note that the center of the maps is removed ($|\lambda| < 10$ km). The isocontours for the energy density have arbitrary units. The prescribed isotropy at the source level is lost when crossing the tropopause. White (dark) areas correspond to waves with high (low) energy.

emerge at large wavenumbers. We observe a k^{-3} shape for the largest wavenumbers (e.g., above 2×10^{-4} cycles m^{-1}) and a clear k^{-2} shape for the intermediate scales. According to one of the existing models for the horizontal wavenumber spectrum [Gardner, 1994], the spectral slope should be -2 down to $h_* = fm_*/N \sim 10^{-6}$ cycles m^{-1} . Our results do not reproduce this behavior even though the predicted transition at $h = m_*$ is captured by the simulations.

[42] In most models, horizontal wavenumber spectra are supposedly isotropic. As far as a strong jet dominates the flow, this hypothesis is likely to be incorrect. It is the reason why we analyzed the azimuth distribution of the wave directions from the 2-D horizontal spectrum in Figure 4.

[43] The maps for such spectra are obtained for wavelengths between 10 and 1000 km as for the 1-D spectra and for adjacent layers. As soon as the rays reach the lower part of the tropospheric jet, a strong filtering effect is produced for the waves which phase speeds match the wind velocity. Therefore, in the lower stratosphere, the emerging wave field is strongly anisotropic with preferred westward propagation.

5.3. Dominant Mechanism for Wave Transport

[44] To identify the mechanism responsible for the shaping of the spectra, we repeated the simulations presented in this study in a windless atmosphere (not shown). In this windless simulation the rays were straight lines, with the sole exception of the tropopause region, where the vertical gradient of the Brunt-Väisälä frequency induces one localized refraction event during the wave propagation. Consequently, the spectral transfers were found to be very small, and the obtained spectra neither exhibited power law tail nor significant changes from the source shape. The spectral

transfer of energy that is observed in the simulations with realistic winds is thus almost entirely due to the inhomogeneities and nonstationarities of the background flow.

[45] Some characteristics of this shaping mechanism can be evidenced by looking at the evolution of the wave packet wavenumbers along the rays. However, since we are analyzing the stationary spectra and their variation with altitude, it is natural to eliminate the time dependence in favor of the altitude dependence in the ray equations. This method helps to evidence the sole variation with altitude. Using the same technique and approximations as Souprayen *et al.* [2001] (i.e., $f \ll \omega \ll N$ and a purely unidirectional background wind U and constant N), we can relate the vertical and time increment along the rays $dz = Nk/m^2 dt$ and can modify equation (2) accordingly:

$$\begin{aligned} \frac{dm}{dz} &= -\frac{m^2}{N} U_z \\ \frac{dk}{dz} &= -\frac{m^2}{N} U_x \\ \frac{d\omega}{dz} &= \frac{m^2}{N} U_l. \end{aligned} \tag{8}$$

[46] Thus the more the vertical wavenumber increases, the more the spectral transfer in vertical wavenumber becomes strong. On the contrary, the spectral transfers in horizontal wavenumbers and intrinsic frequencies do not depend on the wave packet actual horizontal wavenumber or frequency. Consequently, since the waves with the highest energy that control the spectral shapes have vertical wavenumbers close to m_* , at first order, spectral transfers in horizontal wavenumbers and intrinsic frequencies are scale independent.

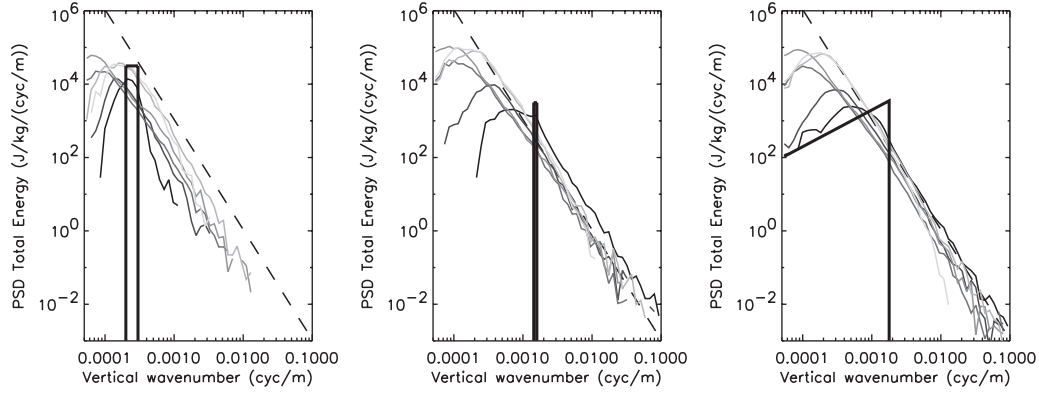


Figure 5. Sensitivity of the resulting spectra with respect to the source distributions. From left to right: Dirac distributions at low wavenumber, at intermediate wavenumber, and large band m^{-1} distribution. The color code for the altitude layers is the same than in Figure 3. The total initial energy is 1 J kg^{-1} for all distributions. See color version of this figure at back of this issue.

Moreover, for realistic values of the a spect ratio U_z/U_x the transfer intensities in the vertical wavenumber direction are expected to be stronger than in the horizontal wavenumber direction, and the winds being dominated by synoptic-scale low-frequency eddies, the rate of transfer along the frequency direction, should also be relatively small.

[47] With these last considerations and the fact that we are using ECMWF analyses that are possibly under-resolving the horizontal and temporal structures of the flow in mind, we will focus our following analysis on the vertical wavenumber energy spectrum. Furthermore, a large part of wave observations relies on vertical soundings, and the particularly well-documented vertical wavenumber spectrum serves as a benchmark for the theory.

6. Focus on the Vertical Wavenumber Spectrum

[48] The results presented in section 5.2 have been obtained with a given uniform source spectrum. We now analyze their robustness with respect to the initial conditions. Then we compare the output from the 3-D simulation with (1) published semiempirical spectral models and (2) the theoretical and analytical model obtained with the stochastic approach [Souprayen *et al.*, 2001].

6.1. Robustness

[49] To test the sensitivity of the vertical wavenumber simulated spectrum to the initial conditions, we report in this section on experiments where the source spectrum has been modified. Actually, the Monte Carlo technique offers the possibility to prescribe various spectral distributions for the source from the same and single numerical experiment: This is realized by changing the initial values for the action (or equivalently energy) of the wave packets. More specifically, we used three distinct source spectra, two delta Dirac distributions $E_i^0 = \omega_i^0 \delta(m_0)$ (with $m_0 = 1.6 \times 10^{-3} \text{ cycles m}^{-1}$ and $m_0 = 2.5 \times 10^{-4} \text{ cycles m}^{-1}$, respectively) and a large-band m^{-1} distribution. We will also study the spectral levels; therefore we prescribe the same total energy per unit mass for each source distribution ($E_t = 1 \text{ J kg}^{-1}$).

[50] The results are reported in Figure 5. Those spectra have to be compared with the one shown in Figure 3. The first significant conclusion is that the m^{-3} tail limit is

reproduced whatever the initial shape. This behavior has been explained in the 1-D stochastic model and results solely from the dispersion-refraction processes of the wave packets. However, the spectral levels in this m^{-3} spectral range varies from one experiment to the other. For the low-wavenumber launch spectrum the refraction process is less efficient, and the tail limit is achieved at higher altitudes. Furthermore, the level is significantly lower than the limit of *Smith et al.* [1987] except for the two uppermost layers. For the high-wavenumber launch spectrum the shaping at large wavenumber is already obtained for the first layer. However, the spectral level for this first layer is higher than the prediction of *Smith et al.* [1987]. It is likely due to the misrepresentation of the dissipation processes at the lower levels, as far as such dissipation is rendered numerically only through the lateral escape of the wave packets from the domain. The escape events only become significant at upper levels.

[51] The spectral shape at low wavenumbers should be sensitive to the launch distribution since wave packets with small wavenumbers have high vertical group velocities and are likely to propagate more freely through the domain than high-wavenumber waves (see equation (8)). However, only the spectra just above the launching altitude seem to be dependent on the source. Indeed, the spectra obtained for the last four layers do not differ from one experiment to the other. It means that the energy in this low-wavenumber portion of the spectra is mainly brought by wavepackets that have been refracted from high wavenumbers.

6.2. Scaling From Empirical Models

[52] In most of the semiempirical models, key parameters are characterizing the shape, magnitude, and variation with altitude of the vertical wavenumber spectrum. Such models provide coherent predictions, namely the scaling of the energy $E(m) \sim N^2/m^3$ for $m > m_*$, where the transition wavenumber is related to the total energy, $m_* \approx \frac{N}{2\pi\sqrt{6Et}}$ [e.g., *Sidi et al.*, 1988]. We provide a comparison between those predictions and our results in Figure 6.

[53] In the plot on the left-hand side the variation with altitude of the energy spectrum is shown. One hundred adjacent layers are selected, and each associated spectrum is shifted such as to verify $E(m_*, z) = 10^2$. The estimate $\frac{N}{2\pi\sqrt{6Et}}$ for m_* , as calculated from the local value of

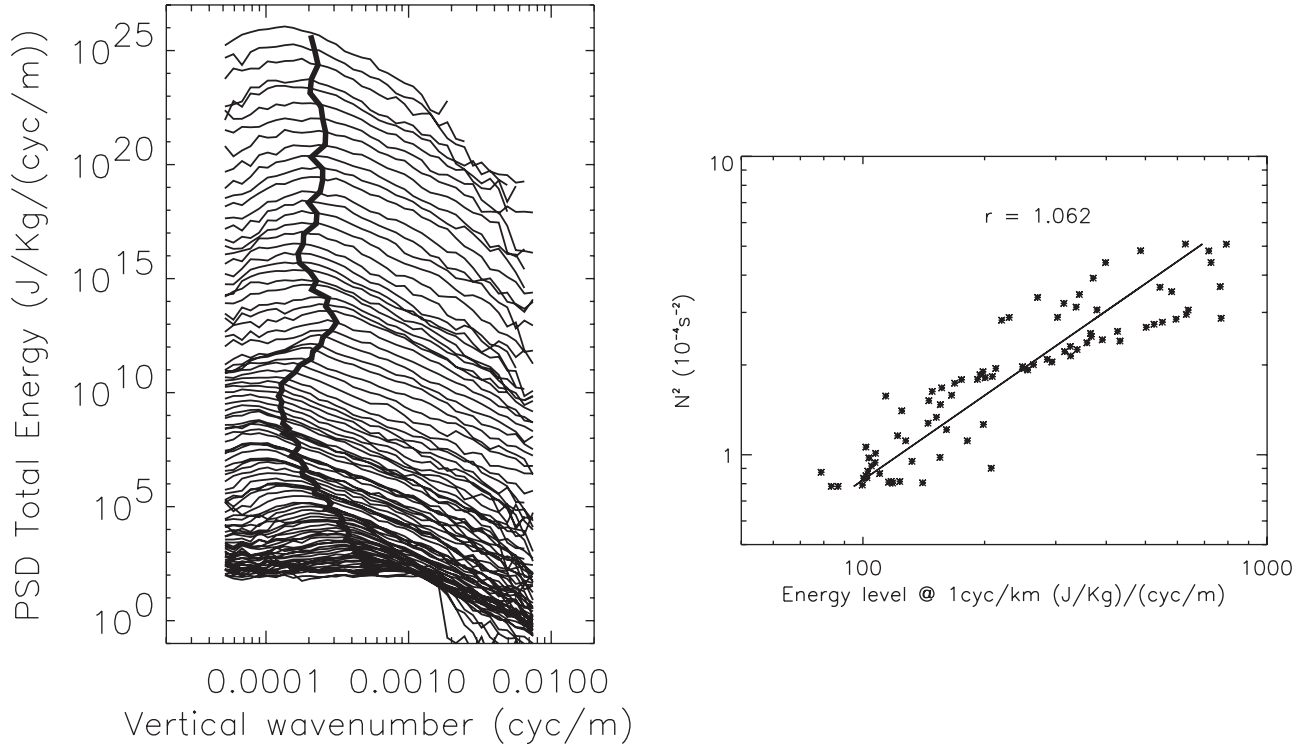


Figure 6. Comparison with the empirical model. (left) Variation of $m_* = \frac{N}{2\pi\sqrt{6E_t}}$ (thick black line) with altitude. (right) Scaling of the saturated spectral level with N^2 . The straight line is a least-square linear fit of the cloud of points. The reported slope is close to 1.

the Brunt-Väisälä frequency and from the total energy deduced by integration of the local spectrum, is shown in the same figure. This value obviously matches the local knee dividing the spectral domains. The m_* variation with altitude can be explained by the opposite effects of (1) the energy increase with altitude and (2) the increase of N around the tropopause. The former is related to the shear-induced diffusion and to density variation. Furthermore, the mean vertical structure of the wind is likely to produce an additional mean Doppler effect on the m_* value.

[54] Owing to the variation of the Brunt-Väisälä frequency from the ground to the middle stratosphere, we can assess the scaling of the spectral magnitude in the m_*^{-3} range with N^2 . The scatterplot $[E(m_* = 1 \text{ cycles km}^{-1}), N^2]$ on the right-hand side of Figure 6 shows the obvious consistency of our simulation with such a prediction; the best least-square linear regression has a 1.1 slope.

6.3. Comparison With the Analytical Stochastic Model

[55] In the study by Souprayen *et al.* [2001] the analytical solution for the 1-D stochastic problem has been given for a delta Dirac source spectrum along with the method to calculate the resulting spectrum for large-band sources. We use this generic shape to try to reproduce the numerical 3-D results. More precisely, the comparisons provided in this section are for the uniform launch spectrum, as given in section 5.2.1. Furthermore, the portion of the spectra that is the most sensitive to the background fields lies in the low wavenumbers. We are going to focus on the shape and variations with altitude of this portion.

[56] The technique to obtain the spectrum at each layer is to convolute the spectrum from the underlying layer with

the generic (transfer) function given in equation (9) of Souprayen *et al.* [2001]. This transfer function depends on two key parameters, the variance of the vertical shear and its correlation length. We are unable to get reliable estimates for such parameters from the 3-DECMWF data; therefore we decided to prescribe ad hoc values for each layer. The results are shown in Figure 7.

[57] The analytical shapes match the numerical results fairly well in the low-wavenumber section. However, there

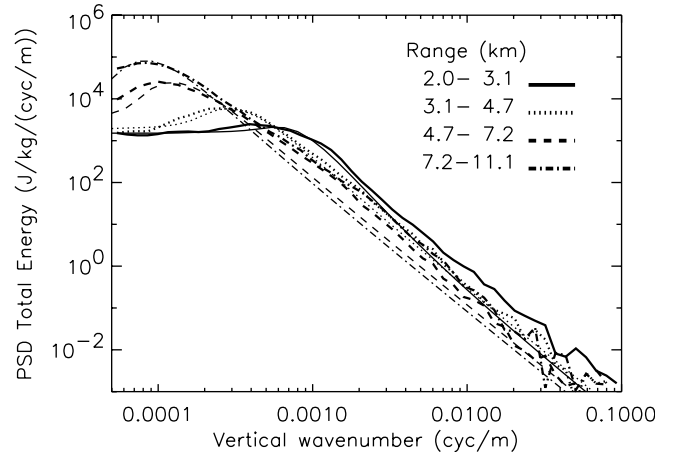


Figure 7. Comparison between the numerical spectra (thick line) with the predicted spectral shapes (thin line) deduced from the analytical 1-D stochastic model Souprayen *et al.* [2001]. We use the same source and layers as in Figure 3. The last, uppermost layers are not shown.

is a discrepancy between the spectral magnitudes in the high-wavenumber tail. Given the over simplifications of the stochastic model (the most important being that the mean background shear is neglected), it is not surprising that we are not able to represent correctly and simultaneously the entire shape of the spectra. For the same reason we have not been able to reconstruct the spectrum for the last uppermost layers (not shown in the plot). Some new modeling efforts are therefore required. Obviously, we must carefully assess the effects of (1) the mean shear, (2) the variations with altitude of the Brunt-Väisälä frequency, (3) the modifications of the shear variance, and (4) its correlation length on the shaping of the wave spectra.

7. Discussion and Summary

[58] Until recently the quasi-universal spectral distributions of the gravity wave energy were explained by saturation concepts where the energy transfer in the wave field is due to convective/dynamical instabilities. Such descriptions lead to generic spectral models that agree with observations, but they suffer several drawbacks or inconsistency that have been underlined by, e.g., *Hines* [1991a]. We try to analyze an alternative process that may explain the shape and intensity of the observed spectra.

[59] We choose to calculate the energy transfer using eikonal techniques, which have been already employed in the frame of oceanic waves [*Heney and Pomphrey*, 1983]. It allows us to estimate the energy and action transfer in the wave field that is produced by off-resonant nonlinear random interactions between scale-separated waves. This approach has been used in a stochastic 1-D model [*Souprayen et al.*, 2001] where successful results for the vertical-wavenumber energy spectra were obtained. In this paper, we complement and confirm those results using numerical simulations in real 3-D and time-varying flows. We simulated the energy transport by randomly launching wave packets from low-level sources and studied the resulting stationary wave field. We calculated the spectral distributions of the energy and analyzed their variations with altitude during the wave propagations away from the sources.

[60] The most significant result obtained from such simulations is that a net energy transport in the spectral domain is observed. This transport is essentially produced by successive refractions of the wave packets in the pseudorandom shears of the flow encountered along the trajectories. Indeed, although the background flow is dominated by large spatial and temporal scales, the Lagrangian trajectories of the wave packets present random characteristics. This process is in close analogy with the classical chaotic advection of tracers in the large-scale stratospheric flow [e.g., *Pierce and Fairlie*, 1993]. More specifically, the dominant mechanism is associated with the vertical shear of the horizontal wind that produces strong refractions of the vertical wavenumber. We show that, regardless of the initial (source) spectral shapes, the vertical wavenumber energy spectra quickly presents the quasi-universal behavior. In particular, the asymptotic m^{-3} tail and the variation with altitude of the characteristic wavenumber (m_*) that are predicted by the semiempirical spectral models [e.g., *Sidi et al.* 1988] are successfully simulated.

[61] As far as horizontal gradients of the flow are taken into account, there is a simultaneous spectral transport along the horizontal wavenumbers (and related along the intrinsic frequencies). However, this transfer appears to be more limited. It could be due to the relatively low horizontal and temporal resolutions of the background fields used in the simulations. Despite this drawback we are able to simulate the azimuth anisotropy of the upward propagating wave field above the dominant tropospheric jet. Preferred westward propagation, as resulting from the filtering of the eastward components by the flow, is usually reported from the observations.

[62] We also attempted a reconstruction of the vertical wavenumber spectrum from the analytical transfer function deduced from the stochastic 1-D model. For an equivalent white noise source spectrum the analytical shapes from the stochastic model and the numerical 3-D simulations are in good agreement. The observed discrepancies are essentially related to the presence of the mean vertical shear of the jet that is not taken into account in the analytical model.

[63] The shaping mechanism of gravity wave spectra that is described in this paper is in close connection with the Doppler-spreading theory (DST) [*Hines*, 1991b]. Yet several discrepancies exist between both approaches. In our approach most of the vertical shear encounters needed for the spectral transfers to occur maybe produced by the sole background flow; in contrast with the DST, waves with large vertical wavelengths are not necessary even though they certainly are responsible for part of the total vertical shear of the horizontal wind. Furthermore, the DST assumes that the shaping of the vertical wavenumber spectrum is quasi-instantaneous, whereas we are able to describe its evolution with altitude (or time). Finally, our results seem to be insensitive to the spectral shape of the source, whereas the resulting spectral slope in the DST depends on the source distribution.

[64] We shall, however, note that our results have been obtained without considering breaking processes, i.e., when the wave amplitude exceeds stability criteria. This obviously must be included in more realistic simulations (note, however, that we used a proxy for wave dissipation at critical levels). In the atmosphere, breaking processes may occur especially at high altitudes, where gravity waves can reach large amplitudes. However, the mechanism considered in this study is ubiquitous and may limit the energy growth. The respective predominance of each process is still an unresolved question, which deserves further numerical studies.

[65] Finally, several aspects of our approach may be improved in the future: (1) the statistics of the transfer rate and its local increase can be used to diagnose the production of turbulent patches, (2) horizontal wavenumber and frequency spectra have to be obtained in simulations with higher resolution background flows, and (3) the analysis of the shear statistics should be considered, as required for a better use of the purely stochastic model.

Appendix A: Conservation Equation for the Wave Action Distribution

[66] A formal derivation of a conservation equation for the distribution of wave action has been obtained in the Lagrangian formalism [see, e.g., *Dewar*, 1970]. This deri-

variation is an extension to multiple random waves of the variational method employed for the single wave by [e.g., *Whitham*, 1970]. Here we give a direct derivation of this extended equation for gravity waves.

[67] We consider that the wave action distribution, i.e. its joint physical and spectral distribution, $\mathcal{A}(\vec{k}, \vec{x}, t)$, is given by the sum over all wave packets of Dirac delta distribution of action located on the dispersion surface in the 6-D phase space

$$\mathcal{A}(\vec{x}, \vec{k}, t) = \sum_w A_w(\vec{x}, t) \delta[\vec{k} - \vec{k}_w(\vec{x}, t)]. \quad (\text{A1})$$

[68] In this linear superposition of wave packets, \vec{k} is a new independent variable. We now search for an evolution equation for \mathcal{A} . The detail of this derivation is given below. (Note that such lifting method holds for any kind of wave-dispersion relation provided that one can construct a conservation equation for a single wave packet and that the weak turbulence approximation is valid.) We begin by differentiating equation (A1) with respect to time,

$$\begin{aligned} \partial_t \mathcal{A}(\vec{x}, \vec{k}, t) &= \sum_w \partial_t [A_w(\vec{x}, t)] \delta[\vec{k} - \vec{k}_w(\vec{x}, t)] \\ &\quad + \sum_w A_w(\vec{x}, t) \partial_t \left\{ \delta[\vec{k} - \vec{k}_w(\vec{x}, t)] \right\} \end{aligned} \quad (\text{A2})$$

$$\begin{aligned} \partial_t \mathcal{A}(\vec{x}, \vec{k}, t) &= \sum_w \partial_t [A_w(\vec{x}, t)] \delta[\vec{k} - \vec{k}_w(\vec{x}, t)] \\ &\quad - \sum_w A_w(\vec{x}, t) \vec{\nabla}_k \left\{ \delta[\vec{k} - \vec{k}_w(\vec{x}, t)] \right\} \cdot \partial_t \vec{k}_w(\vec{x}, t). \end{aligned} \quad (\text{A3})$$

Time derivatives are now eliminated in the right-hand side of equation (A3); we use the last two equations of system 2 for the first and second term,

$$\begin{aligned} \partial_t \mathcal{A}(\vec{x}, \vec{k}, t) &= - \sum_w \nabla_x \left[\vec{\nabla}_{k_w}(\omega_{0w}) A_w(\vec{x}, t) \right] \delta[\vec{k} - \vec{k}_w(\vec{x}, t)] \\ &\quad + \sum_w A_w(\vec{x}, t) \vec{\nabla}_k \left\{ \delta[\vec{k} - \vec{k}_w(\vec{x}, t)] \right\} \\ &\quad \cdot \left(\vec{\nabla}_x \omega_{0w} + \vec{\nabla}_{k_w} \omega_{0w} \vec{\nabla}_x \vec{k}_w \right). \end{aligned} \quad (\text{A4})$$

In the first term of the right-hand side of equation (A4) the Dirac delta function can be included in the divergence operator, provided that the extra term accounting for its derivative with respect to \vec{x} is removed,

$$\begin{aligned} \partial_t \mathcal{A}(\vec{x}, \vec{k}, t) &= - \underbrace{\sum_w \nabla_x \left\{ \vec{\nabla}_{k_w}(\omega_{0w}) A_w(\vec{x}, t) \delta[\vec{k} - \vec{k}_w(\vec{x}, t)] \right\}}_A \\ &\quad + \underbrace{\sum_w A_w(\vec{x}, t) \vec{\nabla}_{k_w}(\omega_{0w}) \cdot \vec{\nabla}_x \left\{ \delta[\vec{k} - \vec{k}_w(\vec{x}, t)] \right\}}_B \\ &\quad + \underbrace{\sum_w A_w(\vec{x}, t) \vec{\nabla}_k \left\{ \delta[\vec{k} - \vec{k}_w(\vec{x}, t)] \right\} \cdot \vec{\nabla}_x \omega_{0w}}_C \\ &\quad + \sum_w A_w(\vec{x}, t) \vec{\nabla}_k \left\{ \delta[\vec{k} - \vec{k}_w(\vec{x}, t)] \right\} \\ &\quad \cdot \underbrace{\left(\vec{\nabla}_{k_w} \omega_{0w} \star \vec{\nabla}_x \vec{k}_w \right)}_D \end{aligned} \quad (\text{A5})$$

[69] In term B the gradient of the Dirac delta function can be expanded using a derivative rule, and this term cancels out exactly with term D . Besides, in term C , $A_w(\vec{x}, t)$ and $\vec{\nabla}_x \omega_{0w}$ are functions of \vec{x} and t only. Both can be included in the ∇_k operator to produce a divergence in wavenumber space,

$$\begin{aligned} \partial_t \mathcal{A}(\vec{x}, \vec{k}, t) &= - \sum_w \nabla_x \left\{ \vec{\nabla}_{k_w}(\omega_{0w}) A_w(\vec{x}, t) \delta[\vec{k} - \vec{k}_w(\vec{x}, t)] \right\} \\ &\quad + \sum_w \nabla_k \left\{ \vec{\nabla}_x(\omega_{0w}) A_w(\vec{x}, t) \delta[\vec{k} - \vec{k}_w(\vec{x}, t)] \right\}. \end{aligned} \quad (\text{A6})$$

Owing to their linearity, the divergence operators can be inverted with the sum

$$\begin{aligned} \partial_t \mathcal{A}(\vec{x}, \vec{k}, t) &= - \nabla_x \left\{ \sum_w \vec{\nabla}_{k_w}(\omega_{0w}) A_w(\vec{x}, t) \delta[\vec{k} - \vec{k}_w(\vec{x}, t)] \right\} \\ &\quad + \nabla_k \left\{ \sum_w \vec{\nabla}_x(\omega_{0w}) A_w(\vec{x}, t) \delta[\vec{k} - \vec{k}_w(\vec{x}, t)] \right\}. \end{aligned} \quad (\text{A7})$$

Furthermore, the multiplicative factors $\vec{\nabla}_{k_w}(\omega_{0w})$ and $\vec{\nabla}_x(\omega_{0w})$ in front of the Dirac delta functions depend on each wave packet component w . However, due to the delta Dirac function property $\int_x f(x_0) \delta(x - x_0) = \int_x f(x) \delta(x - x_0)$, they can be replaced by two k -dependent expressions holding for the whole phase space and identical for all wave packets, namely $\dot{\vec{x}} = \vec{\nabla}_k[\omega_0(\vec{k}, \vec{x}, t)]$ and $-\dot{\vec{k}} = \vec{\nabla}_x[\omega_0(\vec{k}, \vec{x}, t)]$. Therefore those factors can exit the summation, and one finds

$$\begin{aligned} \partial_t \mathcal{A}(\vec{x}, \vec{k}, t) &= - \nabla_x \left\{ \dot{\vec{x}} \sum_w A_w(\vec{x}, t) \delta[\vec{k} - \vec{k}_w(\vec{x}, t)] \right\} \\ &\quad - \nabla_k \left\{ \dot{\vec{k}} \sum_w A_w(\vec{x}, t) \delta[\vec{k} - \vec{k}_w(\vec{x}, t)] \right\}. \end{aligned} \quad (\text{A8})$$

So that, finally,

$$\partial_t \mathcal{A}(\vec{x}, \vec{k}, t) = - \nabla_x [\dot{\vec{x}} \mathcal{A}(\vec{x}, \vec{k}, t)] - \nabla_k [\dot{\vec{k}} \mathcal{A}(\vec{x}, \vec{k}, t)]. \quad (\text{A9})$$

This equation in the augmented phase space describes the conservation of action density for a quasi-linear wave field. It has a similar flux form as the single wave packet in the physical space. However, the velocities account for the position and wavenumber space fluxes. One can use the Hamiltonian structure of the ray equations (equation (2)) to show that this flux-form conservation equation reduces to a Lagrangian conservation along ray paths in the 6-D phase space using $\nabla_x \dot{\vec{x}} = \nabla_x \vec{\nabla}_k(\omega_0) = \nabla_k \vec{\nabla}_x(\omega_0) = -\nabla_k \dot{\vec{k}}$.

Appendix B: Ray Equations

[70] Our numerical experiments are performed in the frame of Boussinesq inertia-gravity waves. We furthermore neglected the vertical component of the wind velocity. Such an approximation has been thoroughly discussed by pre-

Table 2. Characteristics of the Wave Sources for the Caustic Experiment

| Parameter | Value |
|--------------------------------------|---|
| Vertical wavenumber, cycles m^{-1} | $1 \cdot 10^{-4}$ |
| Intrinsic angular frequency | $1.7f$ |
| Azimuth | $0^\circ, 90^\circ, 180^\circ, 270^\circ$ |
| Altitude of launch | 2 km |
| Horizontal launching grid | $4^\circ \times 4^\circ$ |

vious authors [Eckermann, 1997; Walterscheid, 2000]. In this context the ray equation $\left(\frac{d\vec{x}}{dt} = \vec{\nabla}_k \omega_0, \frac{d\vec{k}}{dt} = -\vec{\nabla}_x \omega_0\right)$ reads

$$\begin{aligned}
 \frac{dx}{dt} &= \frac{(N^2 - f^2)km^2}{(k^2 + l^2 + m^2)^2\omega} + u \\
 \frac{dy}{dt} &= \frac{(N^2 - f^2)lm^2}{(k^2 + l^2 + m^2)^2\omega} + v \\
 \frac{dz}{dt} &= \frac{(f^2 - N^2)m(k^2 + l^2)}{(k^2 + l^2 + m^2)^2\omega} \\
 \frac{dk}{dt} &= -\frac{(k^2 + l^2)N N_x}{(k^2 + l^2 + m^2)\omega} - ku_x - lv_x \\
 \frac{dl}{dt} &= -\frac{(k^2 + l^2)N N_y}{(k^2 + l^2 + m^2)\omega} - ku_y - lv_y \\
 \frac{dm}{dt} &= -\frac{(k^2 + l^2)N N_z}{(k^2 + l^2 + m^2)\omega} - ku_z - lv_z.
 \end{aligned} \tag{B1}$$

Appendix C: A Note on Wave Caustics

[71] During the integration of equation (3) the conservation of wave packet total action is used. However, the action density can be undefined at caustics. Formally, caustic encounters happen when the wave volume in physical or spectral space vanishes. If it occurs in the physical space, it corresponds to a caustic, the action density becomes infinite, and dissipation might appear. If it happens in spectral space, it corresponds to a pseudocaustic or shadow region, and the wavepacket is no longer localized. In both cases we cannot use the conservation of total action even though the ray trajectory is correct. We decided to estimate the occurrence of such events using the extended ray tube calculations as did Hayes [1970]. This technique amounts to solve an evolution equation for a tensor $\overrightarrow{\nabla}_a \vec{x}$, whose determinant is the unit volume of a tube around the trajectory (in this notation, a stands for the space coordinates, whereas \vec{x} is the wave trajectory). When reduced to the physical space only, the action density is inversely proportional to this volume. The system that must be solved is

$$\frac{d\overrightarrow{\nabla}_a \vec{x}}{dt} = \overrightarrow{\nabla}_a \vec{x} \cdot \omega_{0xk} + \overrightarrow{\nabla}_a \vec{k} \cdot \omega_{0kk} \tag{C1}$$

$$\frac{d\overrightarrow{\nabla}_a \vec{k}}{dt} = -\overrightarrow{\nabla}_a \vec{x} \cdot \omega_{0xx} - \overrightarrow{\nabla}_a \vec{k} \cdot \omega_{0kx}. \tag{C2}$$

[72] The tensor products on the right-hand side involve the second-order derivatives of the absolute frequencies ω_{0xx} , ω_{0xk} , ω_{0kx} , and ω_{0kk} . Note that the first and last

matrices are symmetric and that ${}^t\omega_{0xk} \equiv \omega_{0kx}$. Let $k_t = \sqrt{k^2 + l^2 + m^2}$, $kh = \sqrt{k^2 + l^2}$, and $R = \frac{k_h^2}{2k_t^2}$ so that

$$\omega_{0x_i x_j} = \frac{R}{\omega^3} \left(N_{x_i x_j}^2 \omega^2 - R N_{x_i}^2 N_{x_j}^2 \right) + k u_{x_i x_j} + l v_{x_i x_j} \tag{C3}$$

$$\omega_{0k x_i} = \frac{km^2 N_{x_i}^2}{\omega^3 k_t^4} [\omega^2 - R(N^2 - f^2)] + u_{x_i} \tag{C4}$$

$$\omega_{0l x_i} = \frac{lm^2 N_{x_i}^2}{\omega^3 k_t^4} [\omega^2 - R(N^2 - f^2)] + v_{x_i} \tag{C5}$$

$$\omega_{0m x_i} = \frac{-mk_h^2 N_{x_i}^2}{\omega^3 k_t^4} [\omega^2 - R(N^2 - f^2)] \tag{C6}$$

$$\omega_{0kk} = \frac{m^2(N^2 - f^2)}{\omega^3 k_t^8} [\omega^2 k_t^4 - k^2 m^2(N^2 - f^2) - 4k^2 \omega^2 k_t^2] \tag{C7}$$

$$\omega_{0kl} = \frac{-klm^2(N^2 - f^2)}{\omega^3 k_t^8} [m^2(N^2 - f^2) + 4\omega^2 k_t^2] \tag{C8}$$

$$\omega_{0km} = \frac{km(N^2 - f^2)}{\omega^3 k_t^8} [2\omega^2 k_t^4 - m^2 k_h^2(f^2 - N^2) - 4m^2 \omega^2 k_t^2] \tag{C9}$$

$$\omega_{0ll} = \frac{m^2(N^2 - f^2)}{\omega^3 k_t^8} [\omega^2 k_t^4 - l^2 m^2(N^2 - f^2) - 4l^2 \omega^2 k_t^2] \tag{C10}$$

$$\omega_{0lm} = \frac{lm(N^2 - f^2)}{\omega^3 k_t^8} [2\omega^2 k_t^4 - m^2 k_h^2(f^2 - N^2) - 4m^2 \omega^2 k_t^2] \tag{C11}$$

$$\omega_{0mm} = \frac{k_h^2(f^2 - N^2)}{\omega^3 k_t^8} [\omega^2 k_t^4 - m^2 k_h^2(f^2 - N^2) - 4m^2 \omega^2 k_t^2]. \tag{C12}$$

The launch characteristics of the wave packets in this experiment are reported in Table 2.

[73] We decided to use parallel wave tubes as initial conditions for all wave packets ($\overrightarrow{\nabla}_a \vec{x}$ and $\overrightarrow{\nabla}_a \vec{k}$ are the

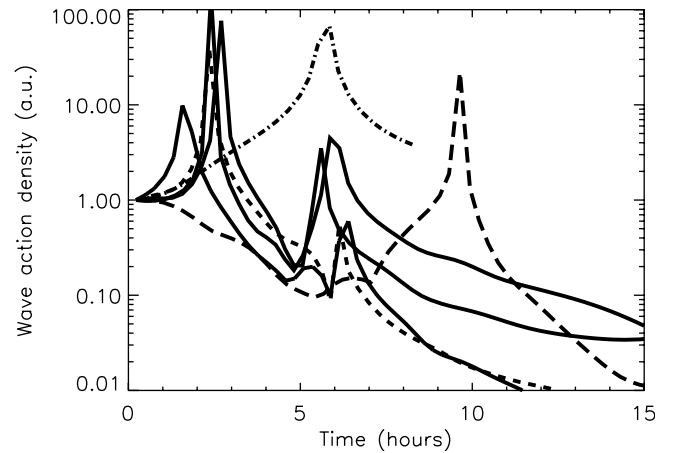


Figure C1. Variation of the wave action density along the path of six arbitrary wave packets as estimated with the ray tube technique. Caustics encounters are associated with the local divergence of the action density, i.e., peaks on the plot.

identity and the null matrices, respectively.) This is a pessimistic situation because one can reasonably suppose that, at the emission, the ray tube should diverge since the wave packet propagates away from the source surface (in most realistic geometry this surface is convex).

[74] As shown in Figure C1, several caustics are detected (1.5 caustic encounter per ray on average). However, we know that an infinite increase of the energy density is not possible. Indeed, Broutman [1986] shows that the increase of amplitude is limited and strongly depends on the initial focusing of the wave packet. We will assume that this increase is weak enough so that breaking or dissipation does not occur. Therefore our estimate for the action transport based on equation (3) will not take into account the possible dissipation at caustics except when the caustic occurs at infinity (i.e., critical layer).

[75] **Acknowledgments.** We would like to acknowledge the European Center for Medium-Range Weather Forecasting for the analyzed winds and temperature fields used in the simulations. First comments on the approach from C. Hines have been helpful in the development of section 2. We would also like to thank M.E. McIntyre for in-depth discussion on wave propagation and dissipation and two anonymous reviewers whose remarks greatly contributed to the improvement of the article. Claude Souprayen received a grant from the European Community, DG XII, during the course of this work (IGWOC, ENV4-CT97-0486).

References

- Allen, J., and R. Vincent, Gravity wave activity in the lower atmosphere: Seasonal and latitudinal variations, *J. Geophys. Res.*, **100**, 1327–1350, 1995.
- Bretherton, F. P., and C. J. R. Garrett, Wavetrains inhomogeneous moving media, *Proc. R. Soc. London, Ser. A*, **302**, 529–544, 1968.
- Broutman, D., On internal wave caustics, *J. Phys. Oceanogr.*, **16**, 1625–1635, 1986.
- Broutman, D., C. Macaskill, M. McIntyre, and J. Rottman, On Doppler-spreading models of internal waves, *Geophys. Res. Lett.*, **24**, 2813–2816, 1997.
- Daubner, S., and V. Zeitlin, On the stationary energy spectra for unidirectionally propagating internal gravity waves, *Phys. Lett. A*, **214**, 33–39, 1996.
- Dewan, E., Saturated-cascade similitude theory of gravity wave spectra, *J. Geophys. Res.*, **102**, 29,799–29,817, 1997.
- Dewan, E., and R. Good, Saturation and the universal spectrum for vertical profiles of horizontal scalar winds in the atmosphere, *J. Geophys. Res.*, **91**, 2742–2748, 1986.
- Dewar, R., Interaction between hydromagnetic waves and a time-dependent inhomogeneous medium, *Phys. Fluids*, **13**, 2710–2720, 1970.
- Dubrule, B., and S. Nazarenko, Interaction of turbulence and large-scale vortices in incompressible 2D fluids, *Physica D*, **110**, 123–138, 1997.
- Dunkerton, T. J., Inertia-gravity waves in the stratosphere, *J. Atmos. Sci.*, **41**, 3396–3404, 1984.
- Dunkerton, T. J., and N. Butchart, Propagation and selective transmission of internal gravity waves in a sudden warming, *J. Atmos. Sci.*, **41**, 1443–1460, 1984.
- Eckermann, S., Influence of wave propagation on the Doppler spreading of atmospheric gravity waves, *J. Atmos. Sci.*, **54**, 2554–2573, 1997.
- Fritts, D., and T. VanZandt, Spectral estimates of gravity wave energy and momentum fluxes, part I, Energy dissipation, acceleration and constraints, *J. Atmos. Sci.*, **50**, 3685–3694, 1993.
- Fritts, D., T. Tsuda, T. Sato, S. Fukao, and S. Kato, Observational evidence of a saturated gravity wave spectrum in the troposphere and lower stratosphere, *J. Atmos. Sci.*, **45**, 1741–1759, 1988.
- Gage, K. S., and G. D. Nastrom, On the spectrum of atmospheric velocity fluctuations seen by MST/ST radar and their interpretation, *Radio Sci.*, **20**, 1339–1347, 1985.
- Gardner, C., Diffusive filtering theory of gravity wave spectra in the atmosphere, *J. Geophys. Res.*, **99**, 20,601–20,622, 1994.
- Garrett, C., and W. Munk, Space-time scales of internal waves: A progress report, *J. Geophys. Res.*, **80**, 291–297, 1975.
- Hayes, W. D., Kinematic wave theory, *Proc. R. Soc. London, Ser. A*, **320**, 209–226, 1970.
- Haynes, P. H., and J. Anglade, Vertical-scale cascade in tracer fields, *J. Atmos. Sci.*, **54**, 1121–1136, 1997.
- Henney, F., and N. Pomphrey, Eikonal description of internal wave interactions—A non-diffusive picture of induced diffusion, *Dyn. Atmos. Oceans*, **7**, 189–219, 1983.
- Hertzog, A., and F. Vial, A study of the dynamics of the equatorial lower stratosphere by use of ultra-long duration balloons, 2, Gravity waves, *J. Geophys. Res.*, **106**, 22,745–22,761, 2001.
- Hertzog, A., C. Souprayen, and A. Hauchecorne, Measurements of gravity wave spectra in the lower stratosphere by Doppler lidar, *J. Geophys. Res.*, **106**, 7879–7890, 2001.
- Hines, C., The saturation of gravity waves in the middle atmosphere, part I, Critique of linear-instability theory, *J. Atmos. Sci.*, **48**, 1348–1359, 1991a.
- Hines, C., The saturation of gravity waves in the middle atmosphere, part II, Development of Doppler-spread theory, *J. Atmos. Sci.*, **48**, 1360–1379, 1991b.
- Pierce, B., and T. Fairlie, Chaotic advection in the stratosphere: Applications for the dispersal of chemically perturbed air from the polar vortex, *J. Geophys. Res.*, **98**, 18,589–18,595, 1993.
- Senft, D. C., C. A. Hostetler, and C. S. Gardner, Characteristics of gravity wave activity and spectra in the upper stratosphere and upper mesosphere at arcibo during early April 1989, *J. Atmos. Terr. Phys.*, **55**, 425–439, 1993.
- Sidi, C., J. Lefrere, F. Dalaudier, and J. Barat, An improved atmospheric buoyancy waves spectrum model, *J. Geophys. Res.*, **93**, 774–790, 1988.
- Smith, S., D. Fritts, and T. VanZandt, Evidence for a saturated spectrum of atmospheric gravity waves, *J. Atmos. Sci.*, **44**, 1404–1410, 1987.
- Souprayen, C., J. Vanneste, A. Hertzog, and A. Hauchecorne, Atmospheric gravity-wave spectra: A stochastic approach, *J. Geophys. Res.*, **106**, 24,071–24,086, 2001.
- Tsuda, T., T. Inoue, D. Fritts, T. VanZandt, S. Kato, S. Sato, and S. Fukao, MST radar observations of a saturated gravity-wave spectrum, *J. Atmos. Sci.*, **46**, 2440–2447, 1989.
- Walterscheid, R. L., Propagation of small-scale gravity waves through large-scale internal wave fields: Eikonal effects at low-frequency approximation critical levels, *J. Geophys. Res.*, **105**, 18,027–18,038, 2000.
- Weinstock, J., Nonlinear theory of acoustic-gravity waves, 1, Saturation and enhanced diffusion, *J. Geophys. Res.*, **81**, 633–652, 1976.
- Weinstock, J., Saturated and unsaturated spectra of gravity waves and scale-dependent diffusion, *J. Atmos. Sci.*, **47**, 2211–2225, 1990.
- Whitham, G., Two-timing, variational principles and waves, *J. Fluid Mech.*, **44**, 373–395, 1970.
- Whitham, G., *Linear and Nonlinear Waves*, 620 pp., Wiley-Interscience, New York, 1974.
- A. Hauchecorne, Service d'Aéronomie du CNRS, Route des Gâtines, BP3, Cedex, Verrières-Le-Buisson F-91371, France. (alain.hauchecorne@aerov.jussieu.fr)
- A. Hertzog, Laboratoire de Meteorologie Dynamique, Ecole Polytechnique, Palaiseau Cedex F-91371, France. (hertzog@lmd.polytechnique.fr)
- C. Souprayen, Centre for Atmospheric Science, DAMTP, University of Cambridge, Silver Street, Cambridge, CB3 9EW, UK. (claudesouprayen@aerov.jussieu.fr)

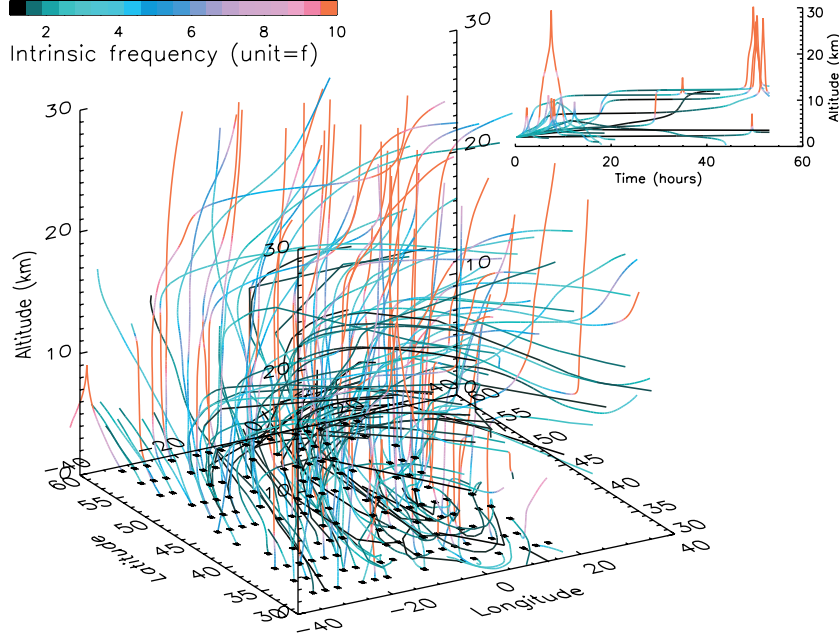


Figure 2. Arbitrary subset (2%) of wave packets trajectories. The crosses at 2 km altitude indicate the source locations, and the color index is related to the wave intrinsic frequencies. Some wave packets are refracted horizontally at the tropospheric jet level and toward low frequencies (shown in black); other waves are refracted toward high frequencies (shown in red) and are propagating freely upward. Upper right corner shows an arbitrary subset of wave packets trajectories $z = f(t)$ that shows vertical reflections.

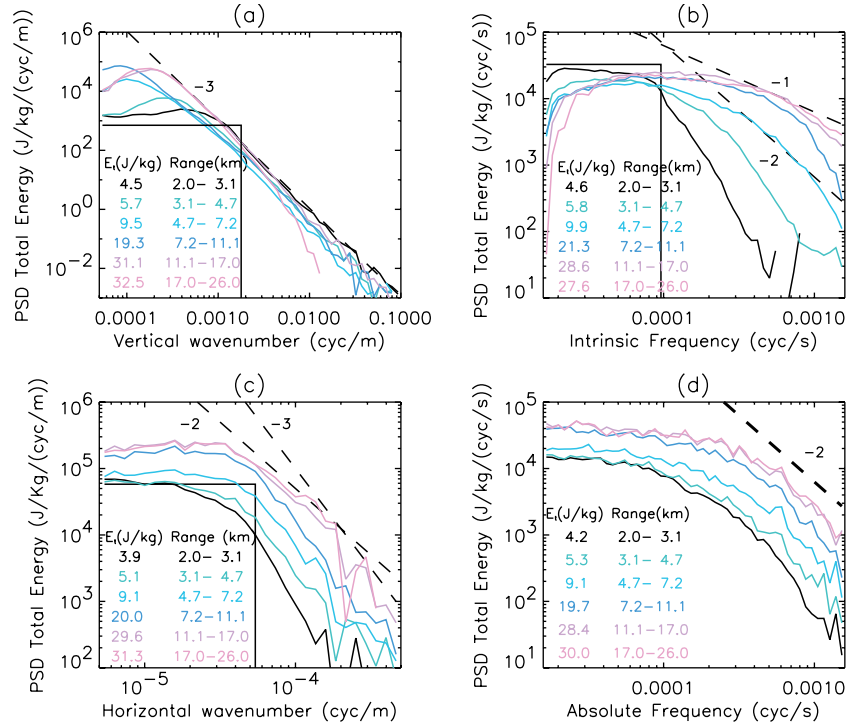


Figure 3. Altitude evolution of the 1-D energy spectra versus (a) vertical wavenumbers, (b) intrinsic frequencies, (c) horizontal wavenumbers, and (d) absolute frequencies. Launch spectra are step functions (solid black line). The colors correspond to the several adjacent vertical layers (whose thickness is increasing). The total energy per unit mass is estimated by integration of the numerical spectrum for each layer. (Note that the total energies slightly differ between each plot since the spectral ranges are not exactly overlapping.) Reference spectra are shown (dashed lines), with slopes detailed in each plot. In Figure 3a there reference spectrum corresponds to the $N^2/6m^3$ tail [Smith et al., 1987].

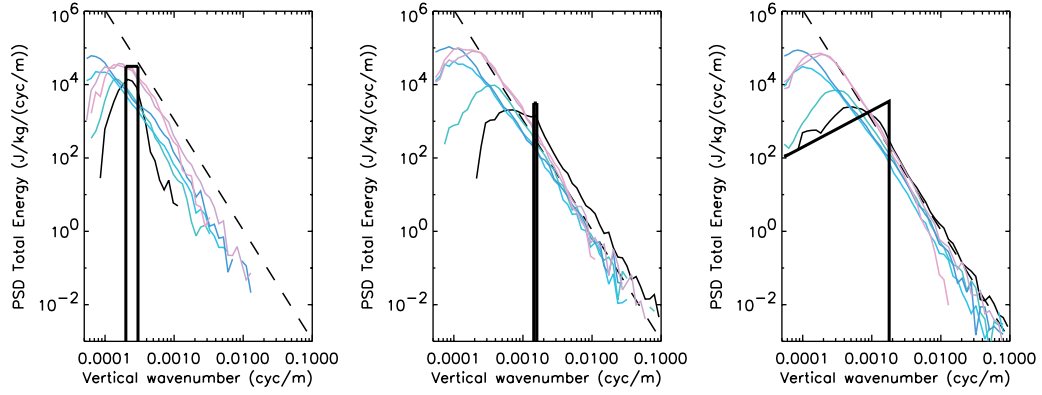


Figure 5. Sensitivity of the resulting spectra with respect to the source distributions. From left to right: Dirac distributions at low wavenumber, at intermediate wavenumber, and large band m^{+1} distribution. The color code for the altitude layers is the same than in Figure 3. The total initial energy is 1 J kg^{-1} for all distributions.